



HAL
open science

Ultrafast Laser-Induced Sub-100 nm Structures on Tungsten Surfaces: Stretched Liquid Dynamics Insights

Priya Dominic, Djafar Iabbaden, Florent Bourquard, Stéphanie Reynaud, Arnaud Weck, Jean-Philippe Colombier, Florence Garrelie

► **To cite this version:**

Priya Dominic, Djafar Iabbaden, Florent Bourquard, Stéphanie Reynaud, Arnaud Weck, et al.. Ultrafast Laser-Induced Sub-100 nm Structures on Tungsten Surfaces: Stretched Liquid Dynamics Insights. Physica Status Solidi A (applications and materials science), In press, 10.1002/pssa.202300703 . hal-04621667

HAL Id: hal-04621667

<https://hal.science/hal-04621667v1>

Submitted on 24 Jun 2024

HAL is a multi-disciplinary open access archive for the deposit and dissemination of scientific research documents, whether they are published or not. The documents may come from teaching and research institutions in France or abroad, or from public or private research centers.

L'archive ouverte pluridisciplinaire **HAL**, est destinée au dépôt et à la diffusion de documents scientifiques de niveau recherche, publiés ou non, émanant des établissements d'enseignement et de recherche français ou étrangers, des laboratoires publics ou privés.

Ultrafast Laser-Induced Sub-100 nm Structures on Tungsten Surfaces: Stretched Liquid Dynamics Insights

Priya Dominic, Djafar Iabbaden, Florent Bourquard, Stéphanie Reynaud, Arnaud Weck, Jean-Philippe Colombier, and Florence Garrelie*


The origin of high-spatial-frequency laser-induced periodic surface structures, known as HSFLs, has always been a controversial topic. HSFLs of sub-100 nm periodicity and sub-20 nm amplitude are generated on tungsten by Ti:sapphire femtosecond laser irradiation under four different processing environments (ambient, air at 10 mbar, Ar at 10 mbar, and vacuum at 10^{-7} mbar). The topography and subtopography analysis together with two-temperature model-molecular dynamics simulations reveal that HSFLs formation originates from laser-induced thermal stresses, implying both surface tension and tensile forces are involved. The experimental observation of subsurface cavitation confirms a hydrodynamics-based origin for these nanostructures.

1. Introduction

Ultrafast laser-induced ripples or laser-induced periodic surface structures (LIPSS) with sizes ranging from few tens of nanometers to micrometers have been extensively studied in recent years because of their universality and vast potential for various industrial applications such as in tribology,^[1,2] photovoltaics,^[3] biomaterials,^[4,5] and so on. Typically, they are divided into two main categories—low-spatial-frequency LIPSS (LSFLs), with period (Λ), $\lambda/2 < \Lambda < \lambda$ (λ is the wavelength of the laser used) and high-spatial-frequency LIPSS (HSFLs), with $\Lambda < \lambda/2$.

P. Dominic, D. Iabbaden, F. Bourquard, S. Reynaud, J.-P. Colombier, F. Garrelie
UJM-Saint Etienne, CNRS, Laboratoire Hubert Curien UMR 5516, Institute of Optics Graduate School
University Lyon
F-42023 St-Etienne, France
E-mail: florence.garrelie@univ-st-etienne.fr

A. Weck
Department of Physics
University of Ottawa
STEM Complex, 150 Louis Pasteur, Ottawa, ON K1L 6N5, Canada

 The ORCID identification number(s) for the author(s) of this article can be found under <https://doi.org/10.1002/pssa.202300703>.

© 2023 The Authors. physica status solidi (a) applications and materials science published by Wiley-VCH GmbH. This is an open access article under the terms of the Creative Commons Attribution-NonCommercial-NoDerivs License, which permits use and distribution in any medium, provided the original work is properly cited, the use is non-commercial and no modifications or adaptations are made.

DOI: 10.1002/pssa.202300703

While it has almost been 50 years since their discovery,^[6] the mechanism of their origin is still under debate.

The origin of LSFLs is usually attributed to electromagnetic models, where the interference of scattered wave or surface polaritons with the incoming laser beam plays a dominant role.^[7] Further, as confirmed by finite-difference time-domain (FDTD) simulations,^[8] Sipe's efficacy theory^[9] of inhomogeneous subsurface energy absorption triggered by surface roughness seems to influence LSFL formation. Hence, it is mostly accepted for LSFLs to have an electromagnetic-based origin. The case of

HSFLs is more complicated with numerous theories like second harmonic generation,^[10,11] variation in optical properties during laser pulse irradiation,^[12] nascent plasma theory,^[13] surface instabilities leading to matter reorganization,^[14] and hydrodynamic instabilities driven by electromagnetics^[15] attempting to explain their origin.

As HSFLs are generally associated with no significant ablation and redeposition,^[16,17] the final topography and subtopography can add to the total story of possible mechanisms involved in their formation. This, together with one of the numerous possible numerical models like FDTD,^[18] particle-in cell,^[19] or hybrid models between two-temperature model and molecular dynamics (TTM-MD),^[20,21] can give a complete picture on thermodynamics conditions fostering periodic nanotopography formation. Among these models, TTM-MD is one of the most relevant to follow the temporal evolution of temperature and pressure into the depth of the target along with the possibility to track structural modifications in 3D space and time.

In this work, we are generating HSFLs on tungsten (W) under four different environments (ambient, air at 10 mbar, Ar at 10 mbar, and vacuum at 10^{-7} mbar). Performing the experiments for laser parameters that generate the same surface topography (HSFLs) under these gaseous conditions will also reveal the role of surrounding gas and pressure conditions influencing the formation mechanism (if any). The topography and subtopography investigations are performed with scanning electron microscopy (SEM), atomic force microscopy (AFM), and scanning transmission electron microscopy (STEM) imaging techniques. This information together with the TTM-MD simulations help us to clarify the formation mechanism of HSFLs on W.

2. Results

2.1. Topography Analysis

The topography results obtained are similar to our previous work reported in ref. [22]. HSFLs, parallel to the laser polarization, are generated for all four different laser processing conditions (ambient, air at 10 mbar, argon at 10 mbar, and vacuum at 10^{-7} mbar) and for the same laser parameters with $F_p = 0.35 \text{ J cm}^{-2}$ and $N = 25$. High-resolution SEM images with inset fast Fourier transform are shown in **Figure 1a–d**. The period (Λ) of the obtained HSFLs are in sub-100 nm range. They vary as $51 \pm 4 \text{ nm}$, $92 \pm 3 \text{ nm}$, $95 \pm 3 \text{ nm}$, and $123 \pm 2 \text{ nm}$ for ambient, air (10 mbar), Ar (10 mbar), and vacuum (10^{-7} mbar), respectively. The amplitude of these high-frequency structures revealed heights as small as 10–20 nm measured by AFM (**Figure 1e–h**). These amplitudes are further confirmed by STEM annular dark field (ADF) cross-sectional images, as shown in **Figure 2**.

2.2. Subtopography Analysis

STEM high-angle annular dark-field (HAADF) cross-sectional images of HSFLs generated in four processing environments (ambient, air at 10 mbar, argon at 10 mbar, and vacuum at 10^{-7} mbar) along with nonirradiated, polished W are shown in **Figure 2i–v**. Subsurface voids or subsurface cavitation can clearly be observed for HSFLs in ambient, air (10 mbar), Ar (10 mbar), and vacuum (10^{-7} mbar) conditions (**Figure 2 ii–v**). These voids are absent for nonirradiated W (**Figure 2i**), thus confirming that their origin is associated with femtosecond (fs) laser–mater interaction.

Depending on the irradiation conditions, the size (diameter) of these voids varies from 5 to 15 nm and seems to appear 13–18 nm below the W surface (measured from the surface to the center of the voids). These voids appear to originate at the bottom of the crests of the nanostructures, and open as they rise

and reach the surface. Interestingly, multiple cavitation with smaller diameters associated with single crests are observed, and these voids seem to appear only below the crests of the HSFLs and not on the troughs. In addition, this trend of subsurface cavitation is seen for HSFLs generated under all gas and pressure conditions, with no significant change in the size of subsurface voids or their respective positions below the W surface. This indicates that the formation mechanism of fs laser-induced HSFLs in W can be generalized irrespective of the gaseous conditions in which they are fabricated.

The observation of subsurface voids on metals has already been reported, but not associated with HSFLs on W. There have been reports of subsurface voids of few hundreds of nm in size as observed by STEM cross-sectional images of laser-irradiated Al target (under vacuum) giving rise to microbumps.^[23] Subsurface voids are seen to be associated with periodic structures in Ni.^[24] These periodic structures are resulted from the interference of near-field scattered waves or superposition of far-field scattered waves (nf_{\parallel} and ff_{\perp} , respectively), with incident laser beam. STEM images of subsurface voids (tens of nm in size), associated with nf_{\parallel} and ff_{\perp} crests, were revealed in this case. In our case, subsurface voids of few nm in size associated with HSFLs on W and observed under four different processing conditions (ambient, air at 10 mbar, argon at 10 mbar, and vacuum at 10^{-7} mbar) are being reported.

While the STEM images of frozen subsurface voids in metals are limited in the literature, the mechanism behind their formation is widely studied using TTM-MD. For example, in Ag, under vacuum conditions, surface swelling due to fs laser irradiation was observed at very small fluences, without significant ablation, and was attributed to subsurface cavitation as confirmed by TTM-MD simulations.^[25] In the fluence regime below the spallation threshold, subsurface voids are the reason for surface swelling for fs laser-irradiated Al by TTM-MD.^[26] In all these cases, the reason for subsurface void formation is attributed to the prespallation regime, where the rarefaction wave (resulting from

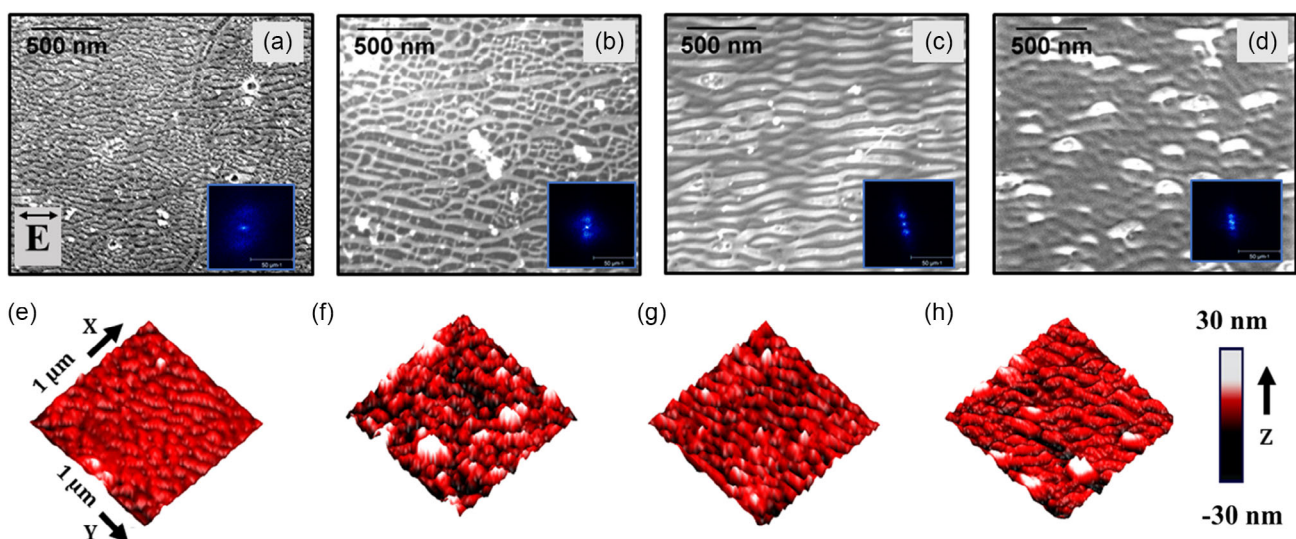


Figure 1. SEM and AFM images of HSFLs generated for $F_p = 0.35 \text{ J cm}^{-2}$ and $N = 25$. a–d) SEM images of HSFLs generated in ambient, air (10 mbar), Ar (10 mbar), and vacuum (10^{-7} mbar), respectively, with inset FFT. e–h) 3D AFM images of HSFLs ($1 \mu\text{m} \times 1 \mu\text{m}$ area) generated in ambient, air (10 mbar), Ar (10 mbar), and vacuum (10^{-7} mbar), respectively.

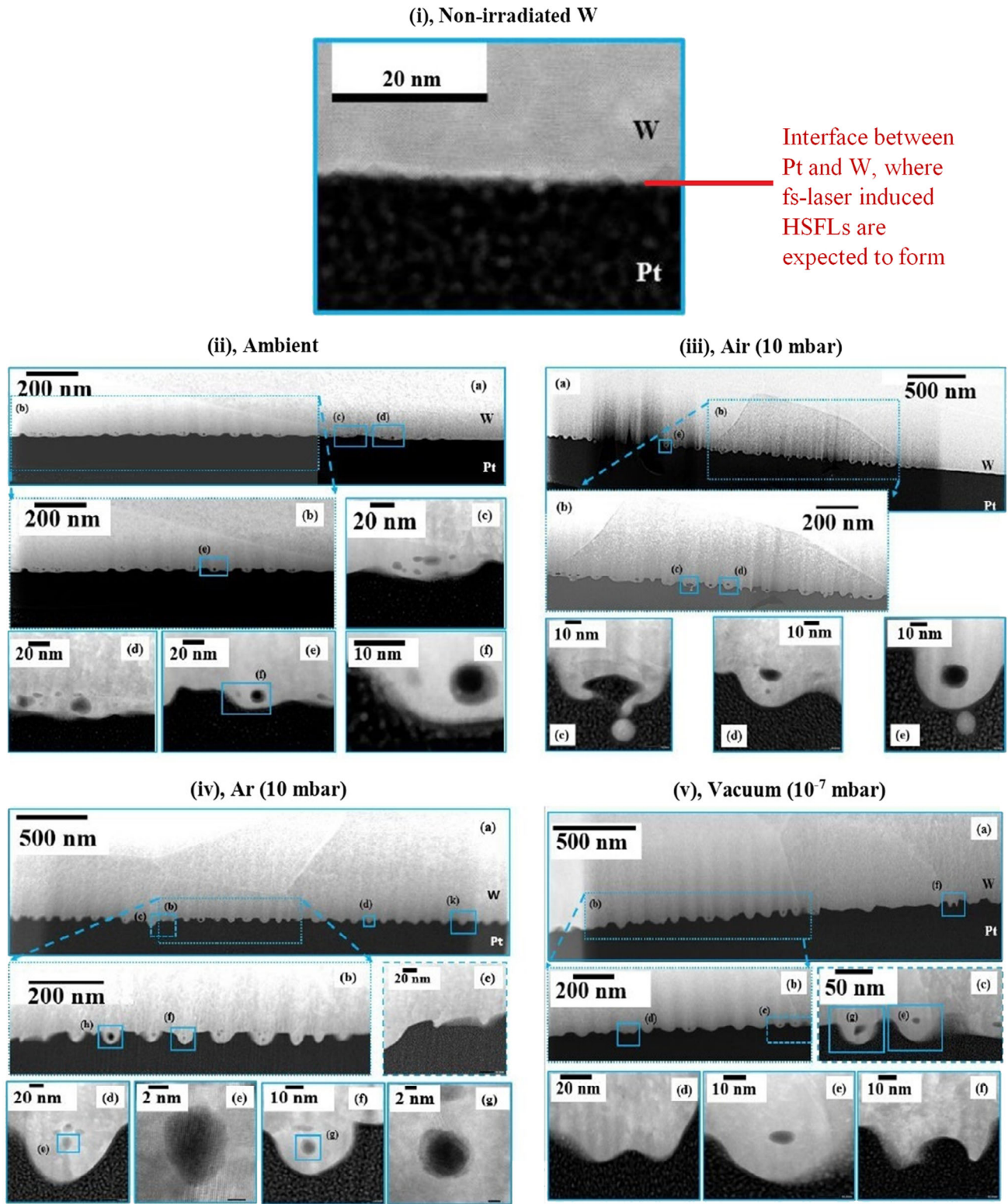


Figure 2. STEM HAADF images of HSFLs (cross section) for i) nonirradiated polished W, and for fs laser irradiated W ($F_p = 0.35 \text{ J cm}^{-2}$ and $N = 25$) showing subsurface cavitations when processed in ii) ambient, iii) air (10 mbar), iv) Ar (10 mbar), and v) vacuum (10^{-7} mbar).

material relaxation) that develops in the laser-induced melt, travelling to the surface of the target, causes the nucleation of the subsurface voids.^[15,24–29] The subsequent fast cooling (10^{12} K s^{-1} for metals^[30]) and solidification trap these cavities under the surface of the material. In another scenario of fs laser irradiation resulting in deformed Al surface,^[31] the experimental results of subsurface cavitations (50–150 nm in diameters) obtained with TEM images are reconstructed by two-temperature hydrodynamics and MD simulations, where the four stages of formation of subsurface voids involving nucleation, formation of cavitation, enlargement, and the compression and deformation during recrystallization of the voids are explained.

To investigate the subsurface voids that we see in W associated with HSFLs, we performed TTM-MD simulations. The subsurface topography evolution of the W interface upon fs laser irradiation at different snapshots of time, as given in **Figure 3a**, indicates that at 10 ps voids form and collapse with a bubble lifetime of 3–10 ps. But after 40 ps, up to 80 ps, voids appear, coalesce, and grow. The smaller voids seem to coalesce together to form larger ones and are observed 25 nm into the W surface. This agrees with our observations and assumptions from the STEM images.

To better understand the influence of fs laser-induced pressure and temperature gradients on subsurface void formation, spatiotemporal evolution of pressure and temperature is tracked

by TTM-MD simulations as shown in **Figure 3b,c**, respectively, for 0–80 ps after the laser hits the surface.

At $t = 1$ ps, W experiences a strong compressive pressure wave at 30 GPa, which decreases to 3 GPa at $t = 40$ ps. As a result of material relaxation, after 40 ps, a rarefaction wave appears with a pressure around -10 GPa (as shown in **Figure 3b** with arrow marks). As subsurface voids also seem to appear after 40 ps, it is reasonable to assume that this rarefaction wave has a major role in the emergence.

When we track the temperature evolution, the maximum temperature achieved for the given laser parameters is 5000 K, which decreases within the depth of W. In the void formation time, i.e., between 40 and 80 ps, the temperature is around 4000 K, which is well above the melting point of W. Hence, we can conclude that the cavitation process takes place when W is in its molten form. The origin of fs laser-induced subsurface cavitation on W can therefore be associated with HSFLs due to the rarefaction wave generated in the molten W, which is later frozen below the crests of HSFLs due to fast resolidification.

In our previous work,^[22] HSFL period was increasing with decreasing atmospheric pressure, which was related to the hydrodynamical-based surface tension-dependent transverse Marangoni gradient process. Therefore, the mechanism underlying the formation of HSFLs can be attributed to the interplay between subsurface cavitation and Marangoni instability.

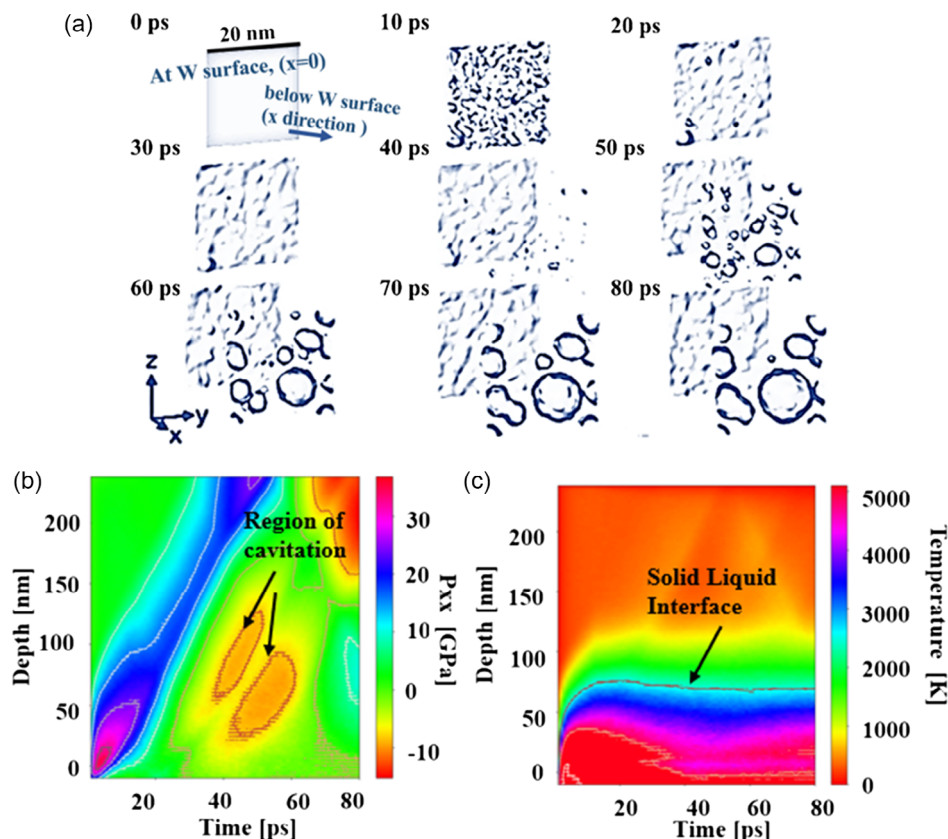


Figure 3. a) Snapshots of voids evolution at several time steps: at 0 ps (corresponding to the W surface at $x = 0$, with no laser irradiation). Time steps at 10, 20, 30, 40, 50, 60, 70, and 80 ps (shows the evolution of the subsurface voids below the tungsten surface in x direction) during ultrafast laser irradiation with a pulse duration $\tau = 60$ fs and an incident fluence $F_{\text{incident}} = 0.35 \text{ J cm}^{-2}$. b) Spatiotemporal evolution of pressure following the x -direction in the W target during void formation. c) Spatiotemporal evolution of temperature in the W target during void formation.

The cavitation observed is a consequence of a thermomechanical effect caused by the intense rarefaction wave. This wave is also recognized for reinforcing the Marangoni convection regime. Therefore, cavitation, although not the primary process in high-spatial-frequency lines (HSFL) formation, serves as a disruptive mechanism, generating nanovoids and nanoreliefs that, in turn, promote convection. The acoustic relaxation of the irradiated target induces hydrodynamic motion within the molten material, thereby playing a crucial role in the formation and elevation of the resulting structure.^[32] In addition, it has already been established for Ni with the help of simulations coupling electromagnetics and hydrodynamics that the rarefaction wave destabilizes the laser-melted nanolayer resulting in Marangoni instability and hence the formation of HSFLs with very small periods and amplitude,^[15] similar to our case of sub-100 nm period and sub-20 nm amplitude HSFLs on W. This and similar studies are well reviewed^[33] where the electromagnetic field enhancement at surface defects, local heat confinement, and the excitation of a subsurface wave triggering Marangoni convection instability is used to explain LIPSS formation resulting in an approach coupling electromagnetic and hydrodynamic principles. Marangoni convection flow of laser melt is also used to explain the origin of fs laser-induced supra-wavelength periodic surface structures on tin, having period larger than the wavelength of the laser used.^[34]

To summarize the formation of HSFLs, under fs laser irradiation W undergoes melting (few tens of nanometers) and is under high compressive stresses, which is followed by a rarefaction wave, causing subsurface cavitation. This destabilizes the molten nanolayer (as this rarefaction wave is directed toward the temperature gradient) giving rise to Rayleigh–B enard–Marangoni instability, redistributing the material from hotter regions (valleys of HSFL) to colder regions (crest of HSFL). The orientation of the HSFLs on W, which are parallel to the direction of light polarization, can be explained with the direction of the fluid flow (created by Marangoni instability) from hotspots located around subsurface voids, which usually results in an orientation parallel to the laser polarization.^[35] Moreover, from the STEM images, it is evident that the formation of HSFLs as a result of Rayleigh–B enard–Marangoni instability due to fs laser-induced compressive stresses, should be applicable for all four different laser irradiation conditions (ambient, air at 10 mbar, argon at 10 mbar, and vacuum at 10^{-7} mbar) irrespective of the gaseous/pressure environments and hence mostly depends upon the laser irradiation parameters.

3. Conclusions

HSFLs generated on W for 60 fs laser irradiation under four different processing environments (ambient, air at 10 mbar, argon at 10 mbar, and vacuum at 10^{-7} mbar) are reported for a laser fluence $F_p = 0.35 \text{ J cm}^{-2}$ and number of laser pulses $N = 25$. The sub-100 nm periodicity and sub-20 nm amplitude of HSFLs are confirmed with SEM and AFM, respectively. The subsurface topography analyzed by STEM HAADF images points out subsurface voids, which are a result of rarefaction wave as confirmed by TTM-MD simulations. The topography, subtopography, and TTM-MD simulations indicate a hydrodynamical

origin of HSFLs based on subsurface cavitation and thermocapillary forces. Specifically, the emergence of HSFLs on W is attributed to the Rayleigh–B enard–Marangoni instability. This thermocapillary phenomenon is intensified by the amplification of surface fluctuations through fs laser-induced tensile stresses generating reported nanocavities. In addition, from the STEM images, we confirm that this mechanism can be generalized for HSFLs formed under various fs irradiation environments, irrespective of the gas and the pressure used, indicating that the formation mechanism of these kind of ripples on W must mainly depend upon the laser parameters.

4. Experimental Section

Laser and Characterization Techniques: Polycrystalline W samples (Goodfellow SARL) with dimensions $10 \text{ mm} \times 10 \text{ mm} \times 1 \text{ mm}$ were electrochemically polished, resulting in an average roughness $R_a \approx 6 \text{ nm}$ as measured by AFM. Polished W samples were irradiated with a linearly polarized laser beam (Titanium-Sapphire, Legend Coherent Inc.) with a central wavelength of 800 nm, pulse duration of 60 fs, and 1 kHz pulse repetition rate, focused with a converging lens of focal length 30 cm down to a focal spot size diameter of $100 \mu\text{m}$ into an ultrahigh vacuum chamber (vacuum processed with a Turbo pump, Agilent Technologies).

W surfaces were irradiated in different atmospheres including ambient, 10 mbar pressure of air and argon (Air products) and under high vacuum (10^{-7} mbar). Using Liu's methods,^[36] the single pulse ablation threshold of our samples was evaluated at a fluence of 0.6 J cm^{-2} . The laser impacts were carried out with a peak fluence $F_p = 0.35 \text{ J cm}^{-2}$ and a number of pulses $N = 25$ in all environmental conditions and the spot size of $100 \mu\text{m}$ is also evaluated by Liu's method.^[36]

While high-resolution SEM (Zeiss Gemini SEM 500 field emission microscope) and AFM (Burker ICON) images were helpful in obtaining topography information, the STEM (JEOL NEOARM, 200 kV Cs-FEG) imaging in the HAADF mode revealed the subsurface topography. In order to accomplish STEM imaging, focused ion beam (FIB) extraction of the lamellae was done for polished, nonirradiated W and for HSFLs produced under the four different processing conditions. Lamellae were prepared with a Pt capping layer by electron beam-induced deposition and topped with a carbon layer by ion beam-induced deposition. Lamellae of dimensions $15 \mu\text{m} \times 2 \mu\text{m}$ were extracted at the center of the laser spot and perpendicular to the orientation of the ripples using FIB milling. Finally, the middle portion of lamellae as long as $3 \mu\text{m}$ was thinned down using ion milling to obtain a thickness $< 100 \text{ nm}$ and render the sample electron transparent.

Hybrid Computational Model: A hybrid simulation coupling two temperature model with molecular dynamics (TTM-MD) simulation scheme implemented in LAMMPS (version 3 March 2020)^[37–44] was used to model an ultrafast laser interaction inducing voids formation within a W target. For this purpose, we started by preparing a perfect initial body-centered cubic W sample with dimensions $l_x \times l_y \times l_z$ of $314 \times 18.2 \times 18.2 \text{ nm}^3$ containing 6 728 000 atoms in a box were selected having periodic boundary conditions following x, y, and z directions, respectively, as shown in **Figure 4**, where the local atomic structure is investigated using the polyhedral template matching algorithm^[45] implemented in the OVITO software.^[46] A structural minimization of the sample was first performed using a force norm criterion of $10^{-6} \text{ eV \AA}^{-1}$. Then, this structure was heated from 0 to 300 K during 15 ps using Nose–Hoover thermostat–barostat style (NPT ensemble). In the present simulations, an embedded atom method interatomic potential developed in ref. [47] and an integrating time step of 1 fs were utilized for both sample preparation and voids formation.

The TTM-MD scheme was solved on a $702 \times 1 \times 1$ electronic mesh, which was applied to the previous configuration (relaxed and thermalized) during 12 ps with W electronic properties input parameters that can be found in the literature.^[44,48,49] The lateral dimensions l_y and l_z were subjected to periodic boundary conditions.

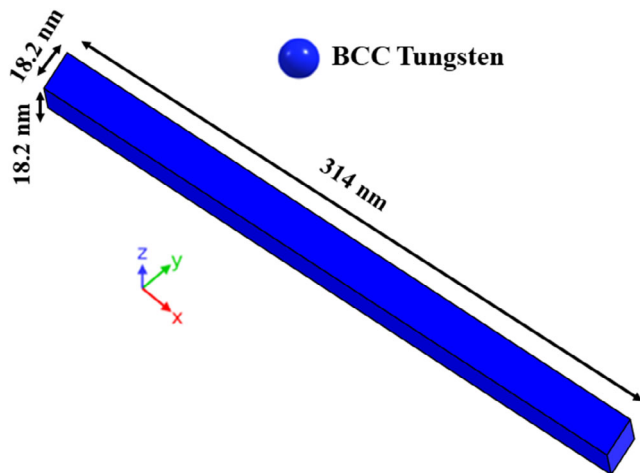


Figure 4. Initial sample geometry used to model ultrafast laser pulse interaction with W target by employing TTM-MD simulations. In blue, it is BCC crystalline structure located inside the rectangular box. The rear region of the sample represents the nonreflecting boundary conditions (NRBC) zone.

During the laser–matter interaction, the lateral dimensions l_y and l_z were subjected to periodic boundary conditions. However, in the x -direction a free boundary condition was created following the laser propagation direction. Moreover, to avoid pressure wave reflection a NRBC with a damping factor $\gamma_{\text{damp}} = 2 \times 10^{-4} \text{ eV ps } \text{Å}^{-2}$ and dimension of $L_{\text{NRBC}} = 63.3 \text{ nm}$ following x was designed at the rear of the target.^[50,51] The laser–matter simulations were performed by employing experimental laser operating conditions of $\tau = 60 \text{ fs}$ pulse duration and $F_{\text{incident}} = 0.35 \text{ J cm}^{-2}$ incident fluence. Finally, the sample was subjected to regular MD in the microcanonical ensemble for 68 ps.

Acknowledgements

The authors acknowledge the Auvergne Rhône Alpes region and the Natural Sciences and Engineering Research Council of Canada (NSERC) along with Mathematics of Information Technology and Complex Systems (MITACS) for funding.

Conflict of Interest

The authors declare no conflict of interest.

Data Availability Statement

The data that support the findings of this study are available from the corresponding author upon reasonable request.

Keywords

femtosecond laser, high-spatial-frequency laser-induced periodic surface structures, hydrodynamic instability, subsurface voids

Received: September 12, 2023

Revised: November 22, 2023

Published online:

- [1] A. Mizuno, T. Honda, J. Kikuchi, Y. Iwai, N. Yasumaru, K. Miyazaki, *Tribol. Online* **2006**, *1*, 44.
- [2] J. Bonse, R. Koter, M. Hartelt, D. Spaltmann, S. Pentzien, S. Höhm, A. Rosenfeld, J. Krüger, *Appl. Surf. Sci.* **2015**, *336*, 21.
- [3] A. Horn, C.-C. Kalmbach, J. G. Moreno, V. Schütz, U. Stute, L. Overmeyer, *Phys. Procedia* **2012**, *39*, 709.
- [4] I. Gnilitzkiy, M. Pogorielov, R. Viter, A. M. Ferrara, A. P. Carapeto, O. Oleshko, L. Orazi, O. Mishchenko, *Nanomed. Nanotechnol. Biol. Med.* **2019**, *21*, 102036.
- [5] N. Gong, N. Maharjan, H. Liu, H. Li, W. Feng, T. L. Meng, J. Cao, C. K. I. Tan, Y. Wei, H. Xie, R. D. K. Misra, H. Liu, *Mater. Technol.* **2022**, *37*, 3089.
- [6] M. Birnbaum, *J. Appl. Phys.* **1965**, *36*, 657.
- [7] F. Keilmann, Y. H. Bai, *Appl. Phys. Solids Surf.* **1982**, *29*, 9.
- [8] J. Z. P. Skolski, G. R. B. E. Römer, J. Vincenc Obona, A. J. Huis in 't Veld, *J. Appl. Phys.* **2014**, *115*, 103102.
- [9] J. E. Sipe, J. F. Young, J. S. Preston, H. M. van Driel, *Phys. Rev. B* **1983**, *27*, 1141.
- [10] A. Borowiec, H. K. Haugen, *Appl. Phys. Lett.* **2003**, *82*, 4462.
- [11] J. Bonse, M. Munz, H. Sturm, *J. Appl. Phys.* **2005**, *97*, 013538.
- [12] Q. Wu, Y. Ma, R. Fang, Y. Liao, Q. Yu, X. Chen, K. Wang, *Appl. Phys. Lett.* **2003**, *82*, 1703.
- [13] A. F. Pan, W. J. Wang, X. S. Mei, H. Z. Yang, X. F. Sun, *Appl. Phys. B* **2017**, *123*, 21.
- [14] J. Reif, O. Varlamova, S. Varlamov, M. Bestehorn, *Appl. Phys. A* **2011**, *104*, 969.
- [15] A. Rudenko, A. Abou-Saleh, F. Pigeon, C. Maclair, F. Garrelie, R. Stoian, J. P. Colombier, *Acta Mater.* **2020**, S1359645420303268, <https://doi.org/10.1016/j.actamat.2020.04.058>.
- [16] G. Li, J. Li, X. Li, Z. Zhu, Y. Hu, J. Chu, W. Huang, presented at the *Inter. Conf. on Optics in Precision Engineering and Nanotechnology (iCOPEN2013)* (Eds: C. Quan, K. Qian, A. Asundi), Singapore, June **2013**, p. 87691V, <https://doi.org/10.1117/12.2021098>.
- [17] D. Zhang, K. Sugioka, RIKEN Center for Advanced Photonics, Wako, Saitama 351-0198, Japan, *Opto-Electron. Adv.* **2019**, *2*, 19000201.
- [18] K. S. Yee, *IEEE Trans Antennas Propag.* **1966**, *14*, 302.
- [19] M. Djouder, T. E. Itina, D. Deghiche, O. Lamrous, *Appl. Surf. Sci.* **2012**, *258*, 2580.
- [20] D. S. Ivanov, L. V. Zhigilei, *Phys. Rev. B* **2003**, *68*, 064114.
- [21] M. V. Shugaev, I. Gnilitzkiy, N. M. Bulgakova, L. V. Zhigilei, *Phys. Rev. B* **2017**, *96*, 205429.
- [22] P. Dominic, F. Bourquard, S. Reynaud, A. Weck, J.-P. Colombier, F. Garrelie, *Nanomaterials* **2021**, *11*, 1069.
- [23] J.-M. Savolainen, M. S. Christensen, P. Balling, *Phys. Rev. B* **2011**, *84*, 193410.
- [24] X. Sedao, A. A. Saleh, A. Rudenko, T. Douillard, C. Esnouf, S. Reynaud, C. Maurice, F. Pigeon, F. Garrelie, J.-P. Colombier, *ACS Photonics* **2018**, *5*, 1418.
- [25] C. Wu, M. S. Christensen, J.-M. Savolainen, P. Balling, L. V. Zhigilei, *Phys. Rev. B* **2015**, *91*, 035413.
- [26] C. Wu, L. V. Zhigilei, *Appl. Phys. A* **2014**, *114*, 11.
- [27] A. Abou-Saleh, E. T. Karim, C. Maurice, S. Reynaud, F. Pigeon, F. Garrelie, L. V. Zhigilei, J. P. Colombier, *Appl. Phys. A* **2018**, *124*, 308.
- [28] L. V. Zhigilei, P. B. S. Kodali, B. J. Garrison, *J. Phys. Chem. B* **1997**, *101*, 8624.
- [29] E. Leveugle, D. S. Ivanov, L. V. Zhigilei, *Appl. Phys. A* **2004**, *79*, 1643.
- [30] W. H. Duff, L. V. Zhigilei, *J. Phys. Conf. Ser.* **2007**, *59*, 413.
- [31] S. I. Ashitkov, N. A. Inogamov, V. V. Zhakhovskii, Yu. N. Emirov, M. B. Agranat, I. I. Oleinik, S. I. Anisimov, V. E. Fortov, *JETP Lett.* **2012**, *95*, 176.
- [32] P. N. Terekhin, J. Oltmanns, A. Blumenstein, D. S. Ivanov, F. Kleinwort, M. E. Garcia, B. Rethfeld, J. Ihlemann, P. Simon, *Nanophotonics* **2021**, *11*, 359.

- [33] J. Bonse, S. Gräf, *Laser Photonics Rev.* **2020**, *14*, <https://doi.org/10.1002/lpor.202000215>.
- [34] D. Zhang, R. Liu, Z. Li, *Int. J. Extreme Manuf.* **2021**, *4*, <https://doi.org/10.1088/2631-7990/ac376c>.
- [35] A. Rudenko, C. Mauchair, F. Garrelie, R. Stoian, J. P. Colombier, *Appl. Surf. Sci.* **2019**, *470*, 228.
- [36] J. M. Liu, *Opt. Lett.* **1982**, *7*, 196.
- [37] Fix TTM command- fix ttm command - LAMMPS documentation. n.d. https://docs.lammps.org/fix_ttm.html (accessed: 27 June 2023).
- [38] D. M. Duffy, A. M. Rutherford, *J. Phys.: Condens. Matter* **2007**, *19*, 016207.
- [39] A. M. Rutherford, D. M. Duffy, *J. Phys.: Condens. Matter* **2007**, *19*, 496201.
- [40] J. K. Chen, D. Y. Tzou, J. E. Beraun, *Int. J. Heat Mass Transf.* **2006**, *49*, 307.
- [41] V. Stegailov, S. Starikov, G. Norman, *AIP Conf. Proc.* **2012**, <https://doi.org/10.1063/1.3686424>.
- [42] V. V. Pisarev, S. V. Starikov, *J. Phys.: Condens. Matter* **2014**, *26*, 475401.
- [43] M. A. Seaton, I. T. Todorov, S. L. Daraszewicz, G. S. Khara, D. M. Duffy, *Mol. Simul.* **2021**, *47*, 180.
- [44] S. L. Daraszewicz, Y. Giret, H. Tanimura, D. M. Duffy, A. L. Shluger, K. Tanimura, *Appl. Phys. Lett.* **2014**, *105*, <https://doi.org/10.1063/1.4890413>.
- [45] P. M. Larsen, S. Schmidt, J. Schiøtz, *Model. Simul. Mater. Sci. Eng.* **2016**, *24*, 055007.
- [46] A. Stukowski, *Modell. Simul. Mater. Sci. Eng.* **2009**, *18*, 015012.
- [47] M.-C. Marinica, L. Ventelon, M. R. Gilbert, L. Proville, S. L. Dudarev, J. Marian, G. Bencteux, F. Willaime, *J. Phys.: Condens. Matter* **2013**, *25*, 395502.
- [48] E. Bévilion, J.-P. Colombier, V. Recoules, R. Stoian, *Phys. Rev. B* **2014**, *89*, 115117.
- [49] N. Stojanovic, D. H. S. Maithripala, J. M. Berg, M. Holtz, *Phys. Rev. B* **2010**, *82*, 075418.
- [50] Fix viscous command — LAMMPS documentation. https://docs.lammps.org/fix_viscous.html (accessed: 27 June 2023).
- [51] L. V. Zhigilei, Z. Lin, D. S. Ivanov, *J. Phys. Chem. C* **2009**, *113*, 11892.